



Large discrepancies of global greening: Indication of multi-source remote sensing data



Zhaoqi Wang^{a,*}, Hong Wang^a, Tongfang Wang^a, Lina Wang^a, Xiang Liu^a, Kai Zheng^a, Xiaotao Huang^{b,c,**}

^a State Key Laboratory of Plateau Ecology and Agriculture, Qinghai University, Xining, Qinghai 810016, China

^b Key Laboratory of Restoration Ecology for Cold Regions Laboratory in Qinghai, Northwest Institute of Plateau Biology, Chinese Academy of Sciences, Xining, Qinghai 810008, China

^c Key Laboratory of Adaptation and Evolution of Plateau Biota, Chinese Academy of Sciences, Xining, Qinghai 810008, China

ARTICLE INFO

Keywords:

Inter-comparison
Uncertainty
Vegetation greening
Global warming

ABSTRACT

Global warming has a great impact on the activities of terrestrial vegetation. A consensus has been reached that the global vegetation is greening from the 1980–2010s. However, the trends of global vegetation are highly uncertain after 2000. Therefore, we used multi-source remote sensing vegetation index (VI), climate data, and Mann–Kendall trend analysis to explore the global vegetation trend and its uncertainty from 2001 to 2016. The effects of climate on the changes in vegetation were also investigated. We found that GIMMS-based VIs exhibited decreasing trends. By contrast, MODIS-based VIs and GLOBMAP LAI tended to increase. Evergreen broad-leaf forest contributed the most to the uncertainty of global vegetation trends, and the uncertainty of December–January–February and September–October–November was higher than that in the other seasons. The correlation of forest VI and temperature was the highest in March–April–May, whereas the correlation of non-forest VI and precipitation was higher than that of the forest. The anomalies of GIMMS-based VIs and mean annual precipitation were more consistent in the evergreen broad-leaf forest, woody savannas, mixed forest, evergreen needle-leaf forest, and deciduous needle-leaf forest than those in biomes under the impact of 2015–2016 El Niño.

1. Introduction

Vegetation is a fundamental component of terrestrial ecosystems and plays an important role in regulating climate change (Bonan, 2008; Cramer et al., 2001; Piao et al., 2011, 2015). Vegetation controls the exchange of carbon, water, and energy between the land and the atmosphere (Bonan et al., 1992), and contributes to valuable ecosystem services (Costanza et al., 1997) as food, fuel, soil, and water conservation. Vegetation is highly sensitive to various factors of the natural environment and human intervention, such as land-use change (Chen et al., 2019). The vegetation structure and function are reflecting the effects of climate change and human activities and have received increasing interest in the context of rapid global environmental changes (Keenan and Riley, 2018; Wang

* Corresponding author.

** Corresponding author at: Key Laboratory of Restoration Ecology for Cold Regions Laboratory in Qinghai, Northwest Institute of Plateau Biology, Chinese Academy of Sciences, Xining, Qinghai 810008, China.

E-mail addresses: wangzhaoqi_818@163.com (Z. Wang), xthuang@nwipb.acs.cn (X. Huang).

et al., 2021; Zhu et al., 2018). Vegetation greenness has been increasing on a global scale in recent decades, and it contributes to an increased terrestrial carbon sink and mitigates global climate change (Wang et al., 2019; Zhu et al., 2018). Therefore, quantifying vegetation change and its interaction with climate is important to assess vegetation degradation (Teng et al., 2020), ecological conservation (Gao et al., 2021; Mashapa et al., 2021), carbon neutrality (Jain et al., 2017), and sustainable economic development (Richards and Belcher, 2020) and to understand the functions of terrestrial ecosystems (Smith et al., 2014).

Inter-annual changes in vegetation are the direct response of vegetation to climate variation. Detecting vegetation changes at the global scale using ground-based observations is difficult due to the heterogeneity of change and the lack of observations that can detect these changes spatially and temporally. Satellite provides evidence of such changes in vegetation and significantly improves our understanding of the interaction between vegetation and climate (Jong et al., 2012; Piao et al., 2011). Spectral vegetation index (VI) derived from the satellite is widely used to measure vegetation dynamics from regional to global scale (de Jong et al., 2011; Fensholt et al., 2012, 2009). Such as Normalized Difference Vegetation Index (NDVI) (Tucker, 1979), Enhanced vegetation index (EVI) (Huete et al., 2002), and near-infrared reflectance of vegetation (NIRv), which is found to be significantly related to solar-induced chlorophyll fluorescence and gross primary productivity (Badgley et al., 2017). Leaf area index (LAI), as an important biophysical parameter of vegetation (Liu et al., 2012; Zhu et al., 2013), is also included in our study. These VIs are not only used to model vegetation productivity (Potter et al., 1993; Sellers, 1992; Wang et al., 2017) and analyze driving forces on land surface dynamics (Pettorelli et al., 2005; Wang et al., 2016) but also as a proxy for identifying the Earth's greening or browning (Jong et al., 2012). Myneni's study is the first to reveal vegetation greening over the Northern Hemisphere (Myneni et al., 1997). Zhu investigated the trends of three long-term LAI products (1982–2009) and concluded that the Earth is greening more than browning (Zhu et al., 2016). At the same time, semi-arid areas across the globe showed the same results during 1981–2007 (Fensholt et al., 2012). The trend analysis of fractional vegetation cover, calculated by GIMMS NDVI, suggested that the global vegetation is turning green from 1982 to 2011 (Wu et al., 2014). We can conclude from these studies that the trend of global greening has reached a broad consensus from the 1980s to the 2000s (Jong et al., 2012, 2013; Liu et al., 2015). The causes are the CO₂ fertilization effect (Zhu et al., 2016), global warming (Keenan and Riley, 2018), nitrogen deposition (Greaver et al., 2016), and human intervention (Chen et al., 2019), and so on.

The alternating sequence trends of vegetation depend on the study period (Jong et al., 2012; Piao et al., 2011), especially the trends of global vegetation are highly uncertain after 2000 (Chen et al., 2019; Yuan et al., 2019). The remote sensing products derived from different satellite sensors may introduce substantial uncertainties to vegetation trends over time. For instance, a comparison study between Moderate Resolution Imaging Spectroradiometer (MODIS) C5 and C6 products concluded that the global vegetation presented a greening trend observed by MODIS-C6 VIs from 2001 to 2015. The browning trends in most of the tropical regions detected by MODIS-C5 might be spurious due to sensor degradation (Zhang et al., 2017). Jiang suggested that large inconsistencies existed in the LAI trend from 2003 to 2011 by comparing four long-term LAI products (GLASS, GLOBMAP, LAI3g, and TCDR) (Jiang et al., 2017). In addition, the studies of VI trend on the regional scale are far more than the global scale from the 2000s to recent years (the year of 2016 or later) (Cho et al., 2017; Liu et al., 2016), which hinders our understanding of the interaction between vegetation and climate.

Reliable VI product is crucial for evaluating vegetation degradation (Lamchin et al., 2020), ecological conservation (Asner and Martin, 2016), modeling carbon cycle (Wang et al., 2017), monitoring land cover dynamics (Song et al., 2018), and ecological environment assessment (Wang et al., 2016). Quantitative evaluation of global satellite VI products is significant to ensure the correct

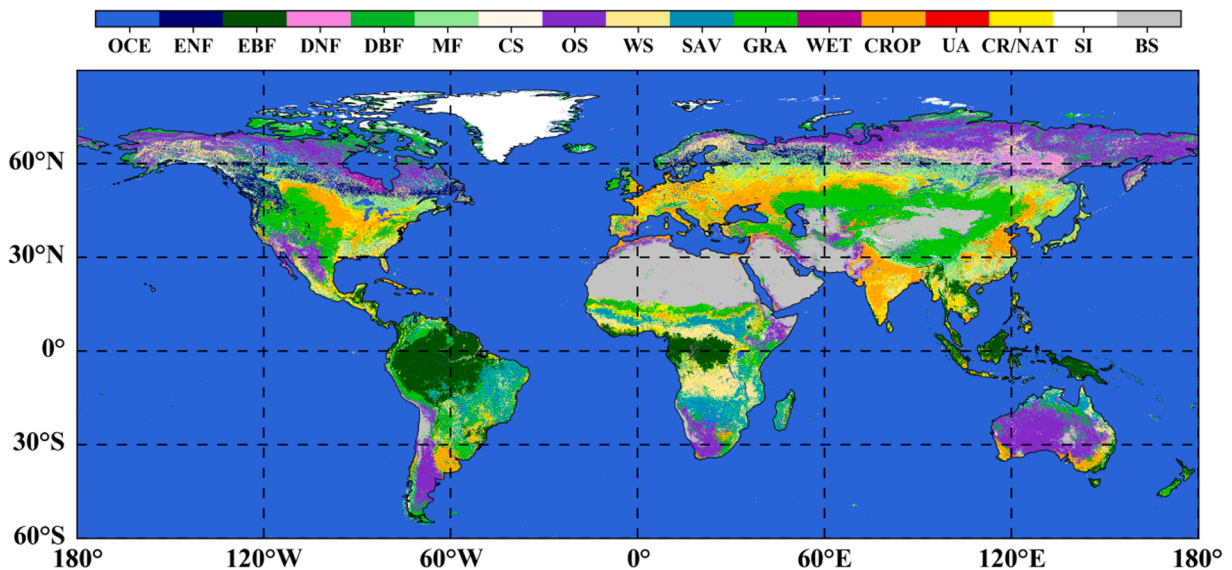


Fig. 1. MCD12Q1 product of 2001 was used to determine the global distribution of biomes. ENF: Evergreen Needleleaf Forest. EBF: Evergreen Broadleaf Forest. DNF: Deciduous Needleleaf Forest. DBF: Deciduous Broadleaf Forest. MF: Mixed Forest. CS: Closed Shrubland. OS: Open Shrubland. WS: Woody Savannas. SAV: Savannas. GRA: Grassland. WET: Wetland. CROP: Cropland. UA: Urban area. CR/NAT: Crop or Nature land. SI: Snow and Ice. BS: Barren or sparse vegetation. OCE: Ocean.

application of VI in scientific research. Moreover, the performance of VI will affect the quality of its derived ecological variables, such as the simulation of gross primary productivity and net primary productivity. Therefore, this study primarily aims to explore the trends of global vegetation and its uncertainty. To accomplish this goal, we evaluated six kinds of satellite-derived VI products (GIMMS LAI, GIMMS NDVI, GLOBMAP LAI, MODIS EVI, MODIS NDVI, and MODIS NIRv) on the consistencies of vegetation trend in annual, seasonal, and monthly at the global scale and analyzed their responses to 2015–2016 El Niño. We hope that this research can provide references for the application of vegetation index and understanding of the interaction between vegetation ecosystems and climate.

2. Materials and methods

2.1. Vegetation map

A MODIS land cover product (MCD12Q1) was used to specify biomes (Fig. 1). This dataset, which includes 17 land cover classes, was developed by the International Geosphere-Biosphere Program (IGBP) Data and Information System. The IGBP classification system was utilized to obtain a land cover map for each year since 2001; thus, the MCD12Q1 production of 2001 was used in this study. The product provides maps of global land cover at a 0.5 km spatial resolution. Furthermore, we resampled the pixel resolution to 0.01° by cubic method and converted the coordinate and projection system to the world geodetic system 1984. At the global and regional scales, the distribution of vegetation and land cover types is qualitatively realistic, and the algorithm performs well (Friedl et al., 2002). The land cover types include Evergreen Needle-leaf Forest (ENF), Evergreen Broadleaf Forest (EBF), Deciduous Needle-leaf Forest (DNF), Deciduous Broadleaf Forest (DBF), Mixed Forest (MF), Closed Shrub-lands (CS), Open Shrublands (OS), Woody savannas (WS), Savannas (SAV), Grasslands (GRA), Wetlands (WET), Croplands (CRO), Urban Area (UA), Cropland or Nature land (CRO/NAT), Snow and Ice (SI), and Barren or Sparse Vegetation (BSV). OCE denotes the ocean in Fig. 1. WET, CR/NAT, UA, SI, and BSV were not considered for analysis because of the small proportion in areas or affected by human management.

2.2. Climate data

Monthly temperatures and precipitation (2001–2016) at a global scale were obtained from the climatic research unit (CRU) higher solution gridded datasets (0.5° × 0.5°) (version 3.24) (Harris et al., 2014) (Table 1). We further resampled the datasets to a spatial resolution of 0.01° × 0.01° by cubic interpolation and composited the monthly data to mean annual temperature (MAT) and precipitation (MAP).

2.3. Remote sensing data

The basic information of the remote sensing-derived VI datasets is shown in Table 1. GIMMS-NDVI (Global Inventory Modeling and Mapping Studies Normalized Difference Vegetation Index) was derived from the AVHRR (Advanced Very High-Resolution Radiometer) sensor mounted on NOAA (National Oceanic and Atmospheric Administration) series satellites. The current GIMMS-NDVI data quality in high latitude areas has been significantly improved compared with the previous version. GIMMS-LAI (Leaf Area Index) data were generated using FFNN (feedforward neural network) algorithm, which is based on GIMMS-NDVI and Moderate Resolution Imaging Spectroradiometer (MODIS) LAI data. Global Mapping (GLOBMAP) LAI version 3 dataset was generated by MODIS and AVHRR data. The relationships between the AVHRR simple ratio and the MODIS LAI were established during the overlapped period (2000–2006). The pixel-based relationship was used to estimate historical AVHRR LAI (1981–2000). Historical AVHRR LAI and MODIS LAI constituted the GLOBMAP LAI data on the entire time sequence (1981–2017). The monthly MODIS VI product (MOD13A3, Collection 6) includes NDVI and Enhanced VI (EVI). The near-infrared reflectance of vegetation (NIRv) is the product of NIR reflectance and NDVI. NIRv was found to be strongly correlated with chlorophyll fluorescence and site-level gross primary productivity (Badgley et al., 2017). The temporal and spatial resolutions of NIRv are consistent with MODIS NDVI and EVI.

In summary, the spatial resolution of all VI data was interpolated to 0.01° (≈ 1.1 km) by using the cubic interpolation method to be consistent with MODIS VI data (the original resolution is 1 km). The study period was set from 2001 to 2016 to facilitate the comparative research because MODIS VI data started in 2001 and GIMMS VI data were only updated up to 2016. At last, we used the

Table 1
Remote sensing and climate data used in this study.

Data	Spatial resolution	Temporal resolution	Sensor	Satellite	References
GIMMS-LAI	1/12° (≈ 9.2 km)	15-day	AVHRR	NOAA	(Zhu et al., 2013)
GIMMS-NDVI	1/12° (≈ 9.2 km)	15-day	AVHRR	NOAA	(Pinzon and Tucker, 2014)
GLOBMAP-LAI	8 km	8-day	AVHRR MODIS	NOAA TERRA	(Liu et al., 2012)
MODIS-EVI	1 km	monthly	MODIS	TERRA	(Huete et al., 2002)
MODIS-NDVI	1 km	monthly	MODIS	TERRA	(Huete et al., 2002)
MODIS-NIRv	1 km	monthly	MODIS	TERRA	(Badgley et al., 2017)
MODIS Land Cover Type (MCD12Q1)	0.5 km	yearly	Combined MODIS	TERRA and Aqua	(Friedl et al., 2002)
Temperatures	0.5°	monthly	–	–	(Harris et al., 2014)
Precipitation	0.5°	monthly	–	–	(Harris et al., 2014)

maximum value composite method (Holben, 1986) to merge the original 15- and 8-day data into monthly, seasonal, and annual data for further analysis.

2.4. Trend analysis

We used the non-parametric Mann–Kendall (M-K) trend test to calculate the trends of six VI products in the growing season (de Jong et al., 2011; Kendall, 1938; Wu et al., 2014). Given (Jiang et al., 2017) the time-series data of x_t ($t = 1, 2, 3, \dots, n$). We detrend the data series of x_t and calculate its auto-correlation coefficient (Gocic and Trajkovic, 2013). The x_t will lose one data due to the first difference transformation performed when to remove autocorrelation in x_t . Therefore, Kadiyala (Kadiyala, 1968) suggested using the following transformation on the first data (x_1).

$$x_0 = \sqrt{1-r^2} \cdot x_1 \quad (1)$$

We supplement x_0 to x_t form new time-series x'_t and resume the trend to x'_t . M-K test was performed on x'_t . The S statistics of the M-K test could be calculated as follows:

$$S = \sum_{i=1}^{n-1} \sum_{j=i+1}^n sgn(x'_{j-i}) \quad (2)$$

where n is the length of data series, and x'_j and x'_i are the data in time series j and i ($j > i$), sgn could be expressed as the following function:

$$sgn(x'_{j-i}) = \begin{cases} +1, & (x'_{j-i}) > 0 \\ 0, & (x'_{j-i}) = 0 \\ -1, & (x'_{j-i}) < 0 \end{cases} \quad (3)$$

The variance is calculated as follows:

$$\text{Var}(S) = n(n - 1)(2n + 5) / 18 \quad (4)$$

The standardized test statistic Z of the M-K test is computed by:

$$Z = \begin{cases} \frac{S-1}{\sqrt{\text{Var}}}, & S > 0 \\ 0, & S = 0 \\ \frac{S+1}{\sqrt{\text{Var}}}, & S < 0 \end{cases} \quad (5)$$

Positive and negative Z indicate increasing and decreasing trends. The $Z_{1-\alpha/2}$ value is 1.960 and 2.576, corresponding to the significant levels of 0.05 and 0.01, respectively.

2.5. Determination of the growing season

The Savitzky-Golay filter is used to smooth the 15-day GIMMS LAI data, which are then interpolated to daily time series by using linear interpolation. The daily LAI data were used to determine the growing season. The start day was determined by LAI greater than 0.1 and increased by 15% of the amplitude of the growing season. By contrast, the end day was determined by LAI value greater than 0.1 and decreased by 15% of the amplitude of the growing season. Therefore, the length of the growing season is the duration between the start and end day. A detailed description could be found in Zhu's study (Zhu et al., 2016).

2.6. Correlation analysis

The correlation between VI and climate data (MAT and MAP) was analyzed using partial correlation from 2001 to 2016. The first step is to calculate the correlation coefficient (r) of the two variables in three variables (VI, MAT, and MAP) as follows:

$$r_{xy} = \frac{\sum_{i=1}^n (x_i - \bar{x})(y_i - \bar{y})}{\sqrt{\sum_{i=1}^n (x_i - \bar{x})^2 \sum_{i=1}^n (y_i - \bar{y})^2}} \quad (6)$$

For example, variables x_i and y_i denote the VI and MAT in year i , respectively. \bar{x} and \bar{y} are the mean values of VI and MAT from 2001 to 2016, respectively. n represents the sum of the ordinal numbers of the year. The same process can be applied to MAT and MAP as well as MAP and VI. The partial correlations are calculated as follows:

$$r_{12,3} = \frac{r_{12} \cdot r_{13} \cdot r_{23}}{\sqrt{(1-r_{13}^2)(r_{23}^2)}} \quad (7)$$

$$r_{13,2} = \frac{r_{13} - r_{12}r_{23}}{\sqrt{(1-r_{12}^2)(r-r_{23}^2)}} \quad (8)$$

$$r_{23,1} = \frac{r_{12} - r_{13}r_{23}}{\sqrt{(1-r_{12}^2)(r-r_{13}^2)}} \quad (9)$$

We suppose that 1, 2, and 3 denote MAT, MAP, and VI, respectively. r_{12} , r_{13} , and r_{23} indicate the correlation coefficients of MAT and MAP, MAT and VI, and MAP and VI, respectively. $r_{12,3}$ is the partial correlation coefficient of MAT and MAP, which removes the effect of VI. $r_{13,2}$ and $r_{23,1}$ have similar meanings.

3. Results

3.1. Trends of vegetation indices

The MODIS-based VIs (MODIS EVI, MODIS NDVI, and MODIS NIRv) and GLOMAP LAI exhibited an increasing trend from 2001 to 2016, the slopes of which reached the significant levels of 0.01 (Fig. 2). By contrast, a decreasing trend of the GIMMS based-VIs (GIMMS LAI and GIMMS NDVI) was observed at the same study period, although the trends were not significant. The inter-annual variation of the vegetation indices formed an obvious peak between 2009 and 2012. After then the MODIS-based VI began to increase, while GIMMS-based VI intended to decrease.

The spatial patterns of the changes in GIMMS based-VIs are shown in Fig. 3a and b. GIMMS LAI showed that 43.9% of the vegetated lands presented an increasing trend that is larger than that observed by GIMMS NDVI (42.4%). These lands were more pronounced in MAM (Fig. S1 q and u), and most of them were mainly found in Alaska, center North America, Europe, the Asia Minor Peninsula, India, and China. The GIMMS-NDVI showed that 57.6% of the vegetated lands had experienced decreasing trend and were more than that of GIMMS LAI observed (56.1%). GIMMS LAI and GIMMS NDVI observed significantly decreased areas accounting for 8.0% and 8.6%, respectively, and most of the vegetated lands with decreasing trends were found in northern North America, tropical forests, and central Asia, which occurred in MAM, SON, and DJF (Fig. S1 q, u, s, t, w, and x). The monthly trend of GIMMS-based VI is shown in Fig. S2 a and b, and the vegetation with decreasing trends occurred in each month, these regions were identified from 15° S to 15° N, and from 60° S to 35° S. By contrast, most of the greening region, observed by MODIS-derived VI and GLOMAP-LAI, were distributed in the northern hemisphere in each month (Fig. S2 c-f).

The spatial patterns of the changes in MODIS based-VIs and GLOMAP LAI are shown in Fig. 3c-f. MODIS EVI observed the most increases in vegetated lands (75.0%) (Fig. 3e), and 11.7% of them reached significance levels of 0.05, followed by MODIS NIRv (74.1%, 10.9% of them are significant) and GLOMAP LAI (73.8%, 15.9% of them are significant) (Fig. 3c and f). MODIS NDVI showed the least increasing areas (73.1%, 14.1% of them are significant) (Fig. 3b). The regions with increasing trends were identified in Europe, the Asia Minor Peninsula, north-central India, and southern and northeastern China. The MODIS-based VIs indicated that the decreasing trend lands were approximately 25%, which is mainly found in western Asia and eastern Brazil Plateau. However, no more than 2% of the lands showed statistically significant decrease. The vegetated lands with increasing trends can be found in MAM, JJA, and SON, whereas the vegetated lands with decreasing trends mainly occurred in JJA (Fig. S3 a-p). The monthly trend of MODIS-based VI and GLBMAP-LAI are shown in Fig. S3 c-f. The vegetation with increasing trends mainly occurred in May to August.

3.2. Uncertainty of the VI trends

The trends of mean annual VI indicated that northwest and center of North America, northern Brazil, Europe, the Asia Minor Peninsula, India, and China exhibited an increasing trend. By contrast, the decreased vegetation trends in the center and western Asia were more than that in the other regions (Fig. 4a). The largest discrepancies of VI were found in Canada, the tropics, and center Russia (Fig. 4b). In general, global vegetation presented an increasing trend in the study period. The mean standard deviation (SD) was the highest in EBF, followed by WS and MF. ENF and DBF have the same SD (Fig. 4c).

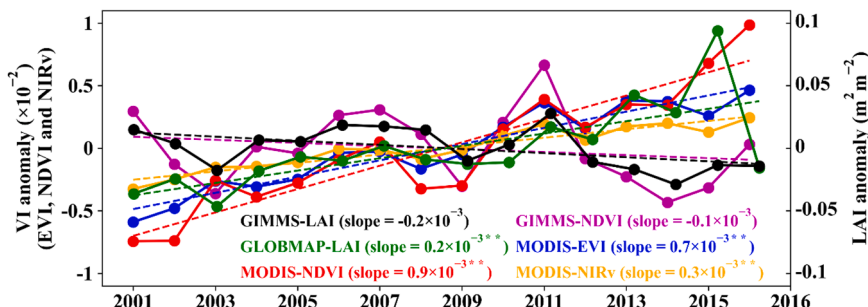


Fig. 2. Linear inter-annual variation trend of vegetation indexes anomaly from 2001 to 2016. The trends are marked with the dashed line, ** denotes the significant changes at a significance level of 0.01.

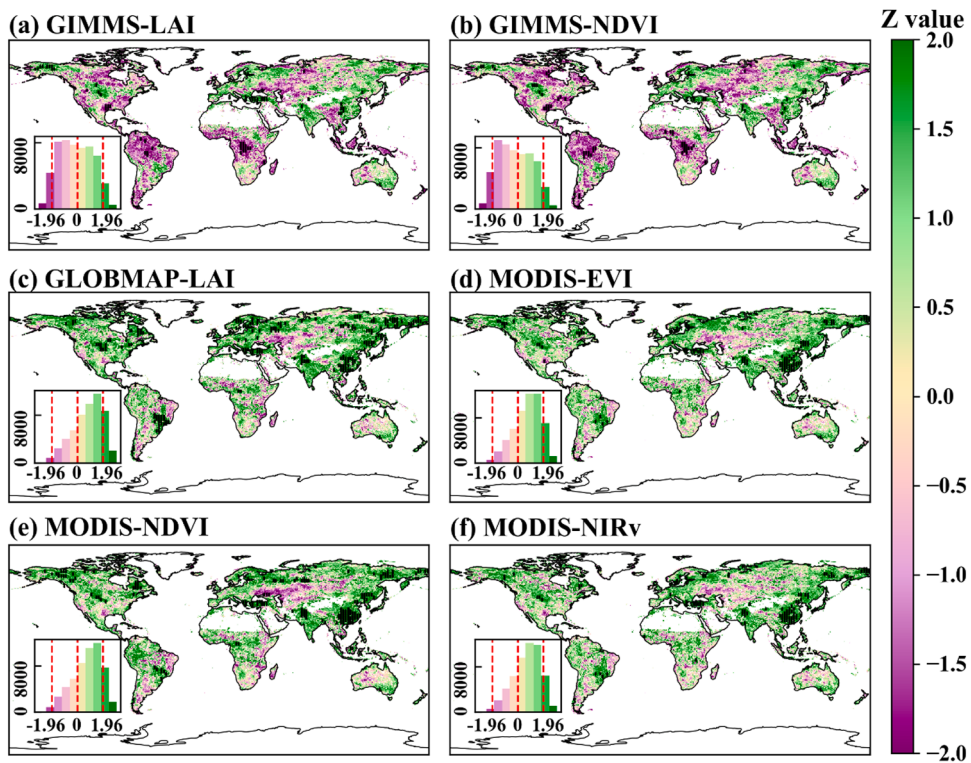


Fig. 3. Spatial pattern of VI trends (a-f) from 2001 to 2016. The regions, showing statistical significance ($p < 0.05$), are marked with black line in each Figure. The lower left sub-Figure denotes the data distribution. The y axis is the pixel numbers, the x axis is the M-K test value, the value is greater than 1.96 or less than -1.96 (marked with red vertical dash line) means statistically significant at the 0.05 level.

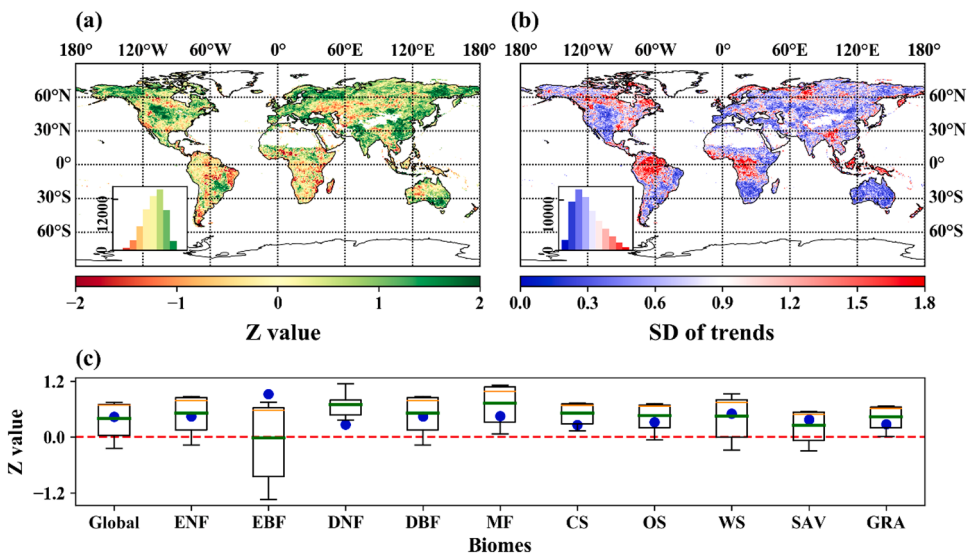


Fig. 4. Spatial pattern of mean annual VI trends (a) and standard deviation (SD) (b) in the growing season from 2001 to 2016. The y axis of the lower-left sub-Figure is the pixel numbers, the x axis of which is the Z and SD value, respectively. Statistics of VI trend across the globe and thirteen biomes as shown in (c). The mean value, quartile, and SD are marked as the green line, orange line, and blue point. (For interpretation of the references to colour in this figure legend, the reader is referred to the web version of this article.)

VI trends exist in large uncertainty in each season (Fig. 5). Globally, the uncertainties of the VI trend in SON and JJA (the mean SD was 0.38 and 0.37) were greater than that in DJF and MAM (the mean SD was 0.36 and 0.28). The uncertainties of seasonal trends in the tropical region were usually greater than that in the other regions. The regions with high uncertainties were also scattered

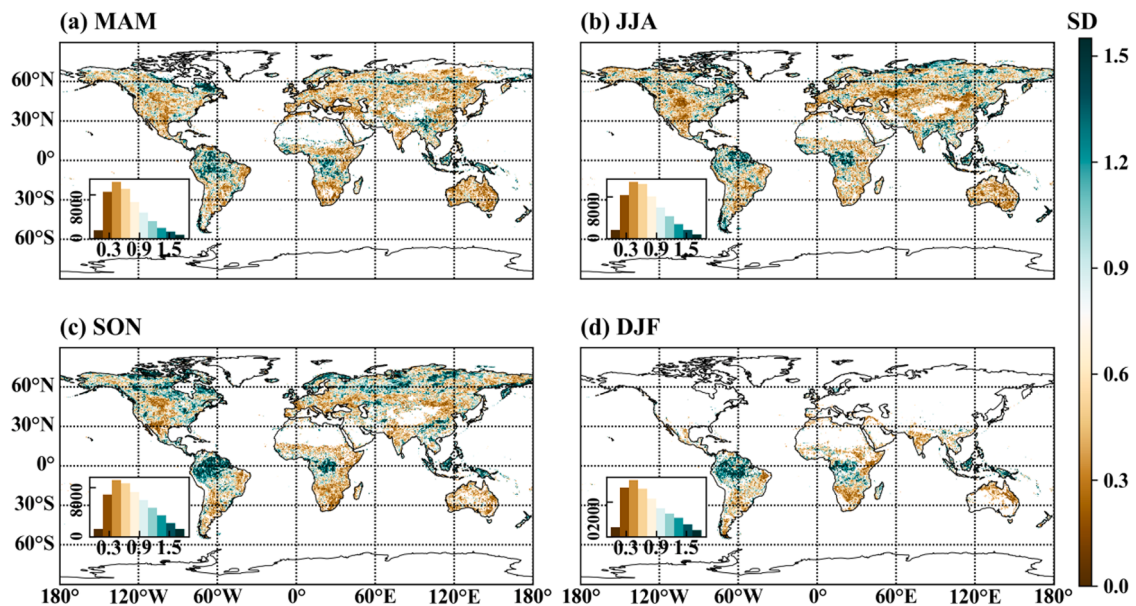


Fig. 5. Spatial pattern of the standard deviation (SD) of seasonal VI trend in the growing season from 2001 to 2016. (a) The SD of VI trend in MAM. (b) The SD of VI trend in JJA. (c) The SD of VI trend in SON. (d) The SD of VI trend in DJF. The y axis of the lower-left sub-Figure is the pixel numbers, the x axis of which is the SD value.

throughout high latitudes in North America and Eurasia (Fig. 5a–c). In each season, the mean SD of the trend in ENF, EBF, DBF, MF, and WS was always greater than that in the other biomes (greater than the black dash line in Fig. S3 a–d).

On the monthly scale, the VI trends were highly uncertain from Apr to Sep in the latitude of 35°S to 60°S (Fig. 6), and the land area is very small in this region (It includes only a part of the southern tip of South America and New Zealand). The VI uncertainties were more pronounced from Jan to Jun in the latitude of 15°S to 15°N, which includes most regions of the tropics. Moreover, the trends of VI are highly uncertain from Jan to Mar and from Sep to Nov in the latitude of 55°N to 75°N.

3.3. Effect of climate factors on the dynamics of VIs

The spatial pattern of the partial correlation coefficient between VIs and climate is shown in Fig. 7. The regions, with a positive correlation between VIs and MAT, were mainly found in high-latitude areas. The VIs, which were negatively correlated with MAT, were located in Australia, the Middle East, the west and south of North America, and most of Africa (Fig. 7a–f). MODIS based-VIs and GLOBMAP LAI were positively correlated with MAT in the tropics. By contrast, the correlations were negative between GIMMS based-VIs and MAT. The VIs were positively correlated with MAP in the west of North America, the Middle East, and a part of southern Asia

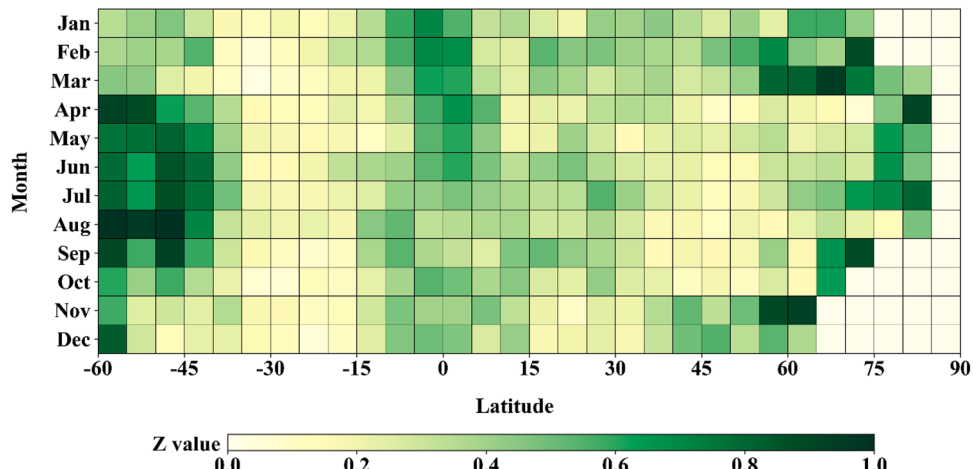


Fig. 6. Uncertainty of VI trend at monthly scale across latitude from 2001 to 2016.

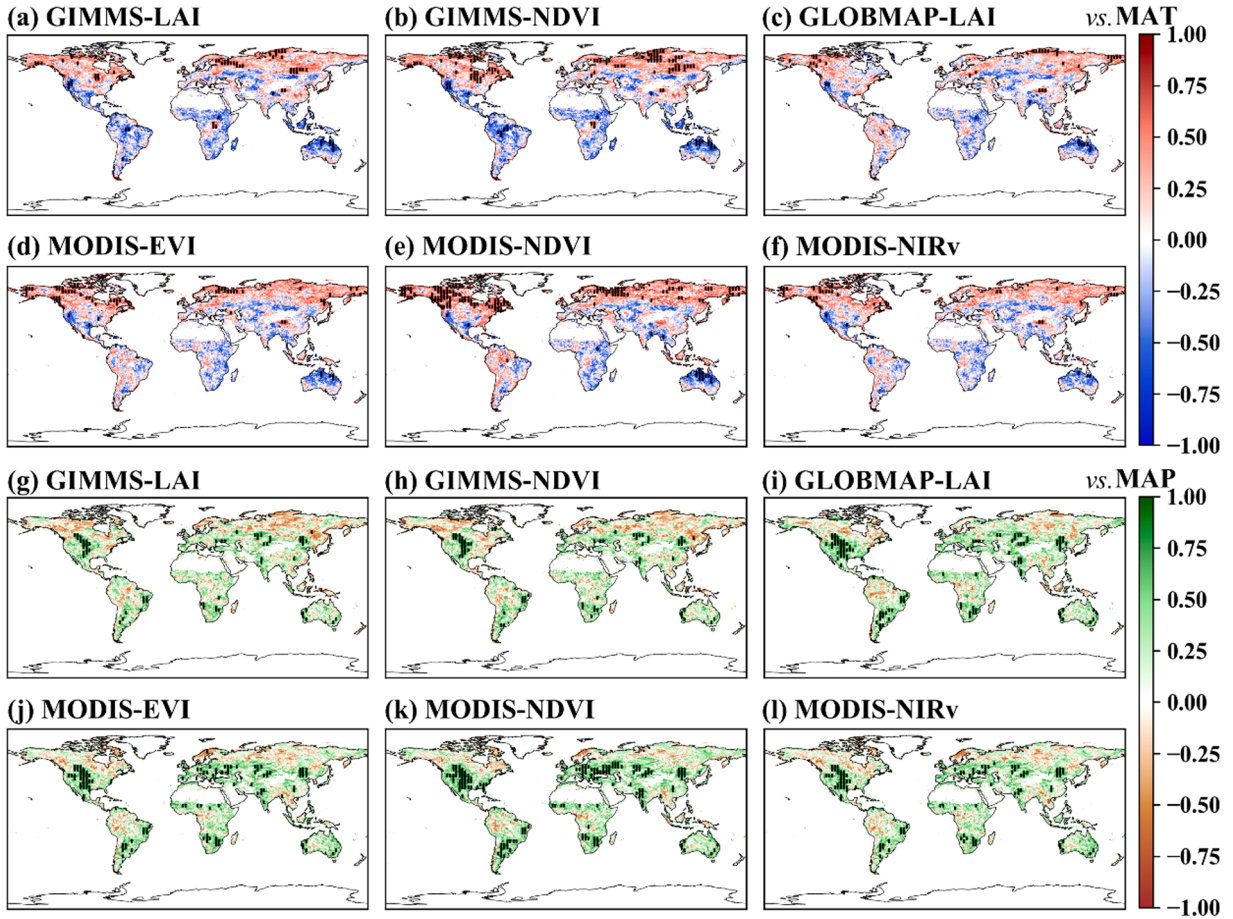


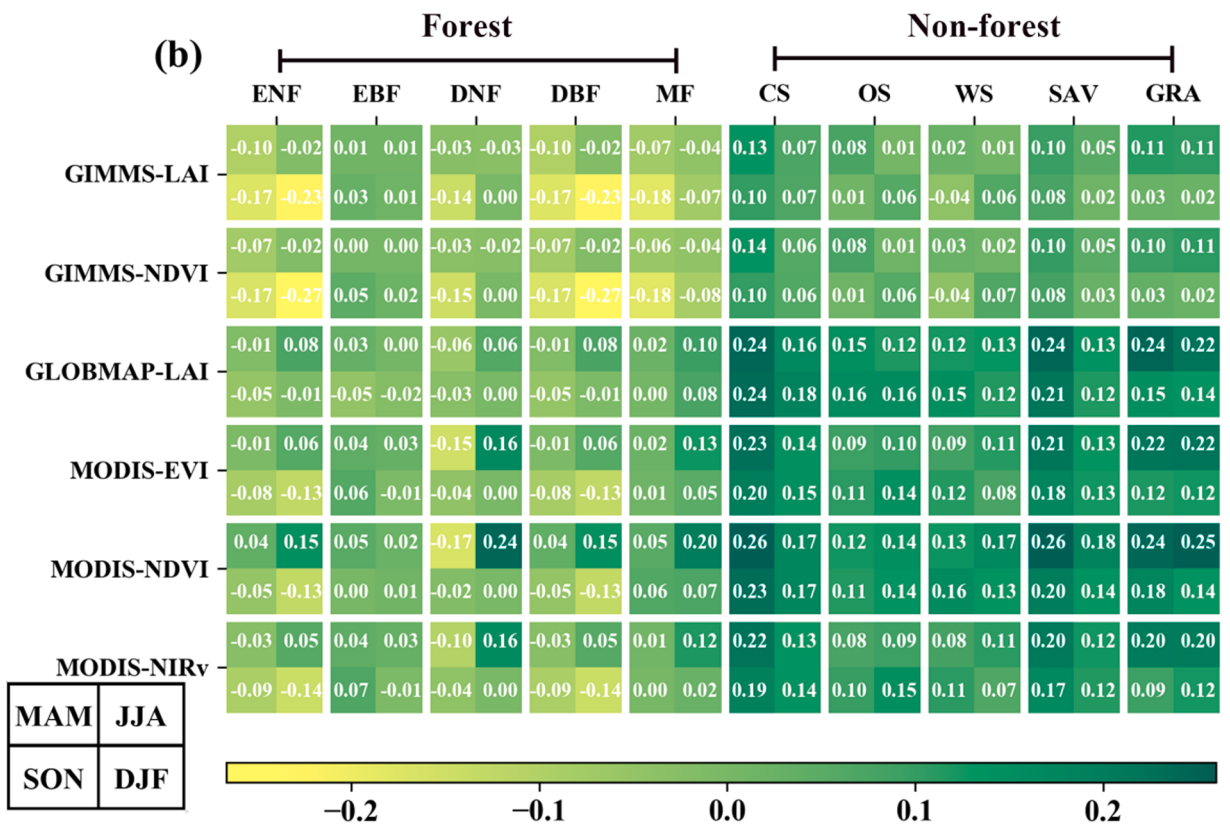
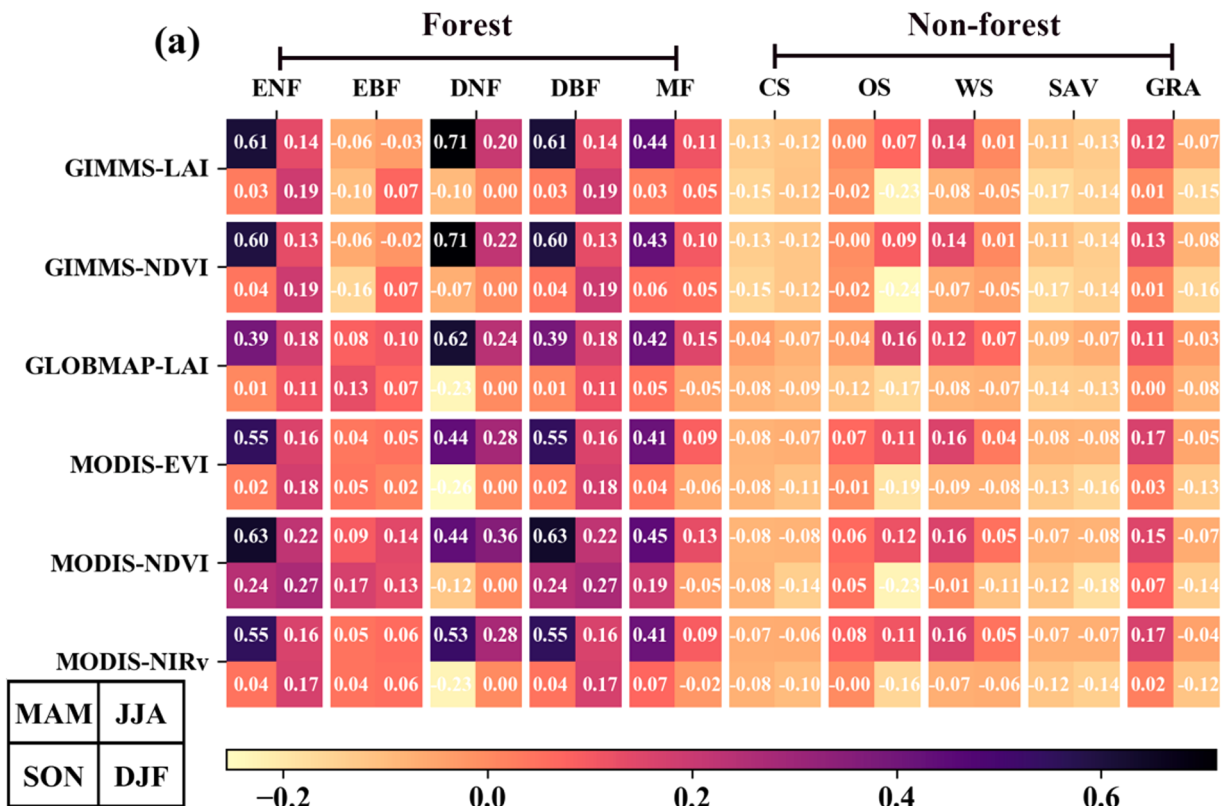
Fig. 7. Spatial pattern of correlation between VIs and climate from 2001 to 2016. The regions, showing statistical significance ($p < 0.05$), are marked with black line in each Figure. The spatial pattern of correlation of VIs and MAT, MAP as shown in (a)-(f) and (g)-(l). The color bar is the correlation coefficient. (For interpretation of the references to colour in this figure legend, the reader is referred to the web version of this article.)

(Fig. 7g-l). The regions that showed a negative correlation between VIs and MAP were found in high-latitude and tropical regions.

Furthermore, we analyzed the correlation between VIs of different biomes and climate factors on the seasonal scale from 2001 to 2016 (Fig. 8). The results of different VIs were consistent, indicating that the correlation between forest VI and temperature in MAM was higher than that in the other seasons, except the biome of EBF. The correlation of non-forest and temperature was not as high as that of forest and temperature (Fig. 8a). Fig. 8b shows that the correlation of non-forest VI and precipitation was higher than that of forest and precipitation, especially in MAM. In contrast, the correlation of MODIS-based VI was higher than that of GIMMS-based VI.

3.4. Response of VI to El Niño in 2015–2016

We compared the mean value of VIs and climate of 2015–2016 to their 14-year average (from 2001 to 2014) to analyze the response of VI to the El Niño event in 2015–2016. Seven of the 10 vegetation types had negative precipitation anomalies. Not surprisingly, the MAT anomaly of nine vegetation types was positive, except DNF. As previously mentioned, the largest SD of VIs was identified in EBF, followed by WS, MF, ENF, and DBF. Therefore, we focused on the analysis of these vegetation types. EBF experienced a strong El Niño in 2015–2016, the MAP anomaly was reached -176 mm/yr , accounting for nearly 9% of the mean annual precipitation from 2001 to 2014 (Fig. 9b). Moreover, the MAT anomaly of 2015–2016 exceeded 0.25°C in EBF. The abnormal climate will inevitably cause adverse effects on the vegetation of EBF. Therefore, the anomalies of GIMMS-LAI, GIMMS-NDVI, and GLOBMAP-LAI were negative in EBF consistent with the anomaly of MAP in 2015–2016. However, the anomaly of MODIS-based VI was not obvious in 2015–2016, implying that the response of EBF was negative to 2015–2016 El Niño under global warming and greening. The anomalies of GIMMS based VIs of WS were consistent with that of MAP, exhibited a negative direction (Fig. 9h). By contrast, the anomalies of the other VIs were opposite to that of MAP, although the MAP anomaly was only 5 mm/yr (Fig. 9e). The anomaly of MAT and MAP was positive in MF under 2015–2016 El Niño. However, their anomaly was no more than $0.2^\circ\text{C}/\text{yr}$ and 10 mm/yr , leading to a small change in the VIs of MF. The MAP anomaly of ENF and DBF was less than -10 mm/yr in 2015–2016, which resulted in their VI anomaly less than 0.05 and 0.1, respectively. The MAP anomaly of SAV (-79.8 mm/yr) accounted for nearly 10% of annual precipitation, which led to



(caption on next page)

Fig. 8. Correlation of VI and mean seasonal temperature (a), precipitation (b) from 2001 to 2016. The value of the upper left, upper right, bottom left and bottom right of each square (surround by the white line) represents the correlation coefficient between VIs and temperature or precipitation in spring, summer, autumn, and winter, respectively (as the low-left insets). The color bar is the correlation coefficient. (For interpretation of the references to colour in this figure legend, the reader is referred to the web version of this article.)

dramatic changes in VI anomaly (Fig. 9i). Therefore, the anomalies of GIMMS-based and MODIS-based VI were consistent with that of MAP in SAV, whereas the response of GLOBMAP LAI to 2015–2016 El Niño seemed not true. The MAP anomalies of DNF, CS, OS, and GRA were no more than 20 mm/yr, which implied that these biomes seem to be less affected by 2015–2016 El Niño (Fig. 9c, f, g, h, and j). The inconsistency of the VI anomaly was probably due to the different sensitivity of vegetation to climate or the degradation of sensors.

4. Discussion

4.1. Trends of vegetation greenness

This study found that GIMMS-based VIs showed decreasing trends of global vegetation. By contrast, MODIS-based VIs and GLOBMAP LAI showed increasing trends from 2001 to 2016. Tropics contributed the most to the uncertainty of global vegetation trends, whether on the scale of annual, seasonal, or monthly. Therefore, the trend of tropical vegetation is the key to determining the greening or browning trend of global vegetation. However, it is a challenge to determine the changes in tropics vegetation remains challenging because of the saturation effect of vegetation index in the regions with high vegetation density; especially, under the influence of clouds and aerosols, little effective information on tropical vegetation is difficult and can be obtained by optical remote sensing (Samanta et al., 2010). Extreme climate events can be used to identify the effectiveness of the vegetation index. A study reported that tropical forests do have responses to the 2015–2016 El Niño event (Wigneron et al., 2020). Therefore, the weak response of vegetation indices to extreme climate may be incorrect.

A previous study reported a detailed comparison analysis of MODIS C5 and C6 products and concluded that the browning trend of tropical vegetation might be spurious due to sensor degradation (Zhang et al., 2017). However, a large proportion of the browning trend of tropical vegetation was identified by GIMMS-based VIs as well as in North America and Indo-China Peninsula. Thus, the spatial distribution consistency of the vegetation browning trend, between GIMMS 3 g and MODIS C5, is a coincidence. By contrast, we agree with Pan's opinion (Pan et al., 2018) that MODIS C6 VIs may overestimate the greening trend of global vegetation and underestimate the browning trend, although their research period is from 2001 to 2013. Regional greening is obvious in the study period, such as China and India. This is consistent with Chen's conclusion (Chen et al., 2019) that China and India lead to greening the Earth.

4.2. Responses of tropical vegetation to climate extremes

Resistance expresses the ability of vegetation to withstand environmental disturbances (De Keersmaecker et al., 2015). In general,

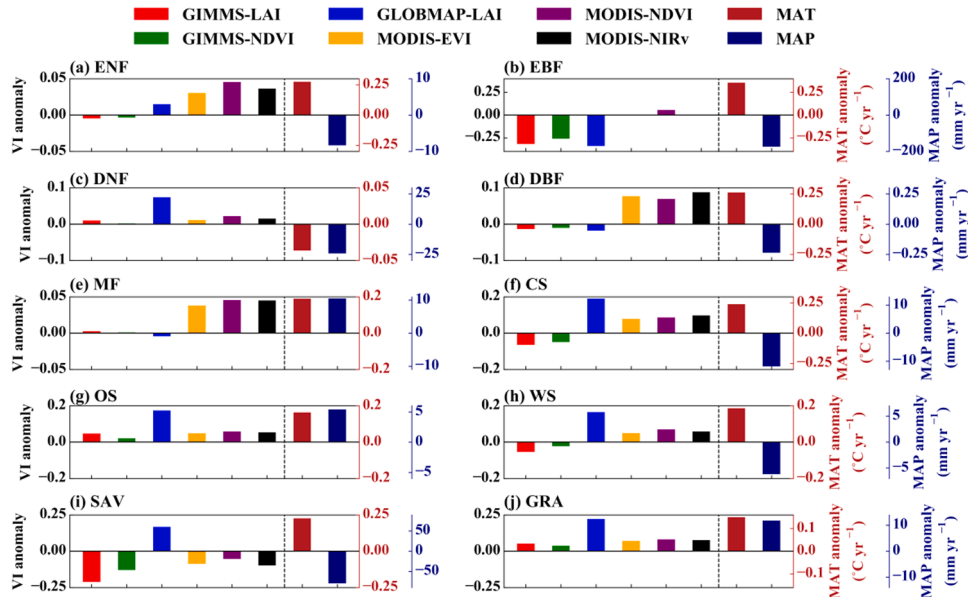


Fig. 9. Anomaly of VIs and climate in 2015–2016 El Niño. The anomaly values of VIs and climate were obtained using the mean value of 2015–2016 abstract which of 2001–2014.

vegetation is resistant to the impact of adverse climates and maintains its normal metabolism (Ciemer et al., 2019). Therefore, it is difficult for remote sensing to detect the responses of vegetation to extreme climates from the appearance of vegetation. The 2015–2016 El Niño is one of the strongest El Niño events in the modern record (Luo et al., 2018); a question raised here is whether tropical vegetation responds to the 2015–2016 El Niño event.

Several studies indirectly proved that tropical vegetation has a strong response to the impact of the 2015–2016 El Niño event. For instance, tropic photosynthesis decreased in 2016 based on an ensemble of six remote sensing models (Luo et al., 2018). van Schaik's study concluded that the 2015–2016 El Niño event caused a reduction in GPP in Amazon compared with the 2007–2014 average (van Schaik et al., 2018); soil moisture shows large reductions across the north-eastern part of the Amazon basin, and Wigneron reported that tropical forests did not recover from the strong 2015–2016 El Niño event by analyzing the above-ground carbon stocks (Wigneron et al., 2020). The tropical biosphere released 2.5 ± 0.34 Pg of carbon into the atmosphere more than in 2011 under the impact of warmer and drier climate that induced by the 2015–2016 El Niño event (Liu et al., 2017). We also found that the negative anomalies of GIMMS-based VI are consistent with the anomaly of MAP (which is up to 200 mm), such a water deficit is bound to cause drought and lead to decreases in vegetation greenness. By contrast, a weak response of MODIS-based VI was identified to 2015–2016 El Niño, even a slight increase in MODIS-NDVI, which implied that GIMMS-based VI may correctly describe the response of vegetation to El Niño, at least in tropics.

4.3. Primary factor on the uncertainties of VI trends

Several factors were considered to be related to global greening, such as land-use changes, climate change, and CO₂ fertilization (Piao et al., 2020). Our study confirmed that China and India contributed most of the global greening because of the increase in forest and farmland, which is also can be attributed to land-use change (Chen et al., 2019). Deforestation, shifting agriculture, and wildfires can be the primary drivers on land-use change in tropics regions from 2001 to 2015 (Curtis et al., 2018), which results in a decline in tropic vegetation greenness. The land cover is fixed throughout our analysis, which will ignore the uncertainty caused by the change in vegetation types. Human activities and climate change will have an impact on changes in vegetation types. However, it is very difficult to quantitatively assess the driving forces, especially the parts that are difficult to explain in the assessment results. Considering the complexity of vegetation type changes, it is difficult to explain clearly in this study. Therefore, we chose to use only one year of land cover data for analysis.

The impacts of climate change on vegetation greenness were varied between regions. We found a positive correlation between global warming and greening in high latitudes, which is consistent with the conclusion of previous studies that global warming promoted vegetation greenness by enhancing metabolism and extending the growing season (Lucht et al., 2002; Mao et al., 2012). Conversely, the temperature in the tropics is close to the optimum temperature of their vegetation, and any excessive warming may reduce vegetation growth in the region (Corlett, 2011). On seasonal scale, we found a strong positive correlation between temperature and forest greening in spring, this was confirmed by a seasonally asymmetric warming experiment that bud-burst and leaf unfolding responded more strongly to spring warming (Yan et al., 2020). While the sensitivity of non-forest VI to precipitation was higher than that of the forest because most of this region is dominated by semi-arid ecosystems, where precipitation is the main driving factor of greening and browning.

Substantial uncertainties remain in the estimation of tropical vegetation greenness. In addition to the driven factors mentioned in land-use change, modeling studies (Los, 2013; Sitch et al., 2015) and free-air CO₂ enrichment experiments (Dubey et al., 2015) support that CO₂ fertilization is a major factor driving global vegetation greening, especially in tropic regions (Hickler et al., 2008; Zhu et al., 2016). However, the effect of CO₂ fertilization may be influenced by climate extremes. Therefore, the drought of the tropics is likely to offset the increase of vegetation greening caused by CO₂ fertilization, a quantitative description of the offset between drought and greenness is still unclear.

5. Conclusion

There were large discrepancies exists in global VI products from 2001 to 2016. Tropics (EBF) contributed the most to the uncertainty of global vegetation trends. The uncertainties of vegetation trend were higher in SON and JJA, than that in DJF and MAM. The regions, with a positive correlation between VIs and MAT, were mainly found in high-latitude areas. Whereas VIs was negatively correlated with MAT in Australia, the Middle East, the west, and the south of North America, and most parts of Africa. The correlation between forest VI and temperature was the highest in MAM, whereas the correlation between non-forest VI and precipitation was higher than that of the forest. The anomaly of GIMMS based-VIs was more consistent with that of precipitation under the impact of El Niño in 2015–2016 in EBF, implying that GIMMS-based VIs were likely correct at least in EBF. MODIS-based VIs may overestimate the greening trend of global vegetation and underestimate the browning trend.

Declaration of Competing Interest

The authors declare that they have no known competing financial interests or personal relationships that could have appeared to influence the work reported in this paper.

Acknowledgments

This research was funded by the National Natural Science Foundation of China (Grant No. 32160278); the Open Project of State Key Laboratory of Plateau Ecology and Agriculture, Qinghai University (Grant No. 2020-ZZ-14, 2021-KF-08); the National Natural Science Foundation of China (Grant No. NSFC32001188); the Natural Science Foundation of Qinghai Province of China (Grant No. 2021-ZJ-973Q); the National Natural Science Foundation of China (Grant No. 42067070).

Appendix A. Supporting information

Supplementary data associated with this article can be found in the online version at doi:[10.1016/j.gecco.2022.e02016](https://doi.org/10.1016/j.gecco.2022.e02016).

References

- Asner, G.P., Martin, R.E., 2016. Spectranomics: emerging science and conservation opportunities at the interface of biodiversity and remote sensing. *Glob. Ecol. Conserv.* 8, 212–219.
- Badgley, G., et al., 2017. Canopy near-infrared reflectance and terrestrial photosynthesis. *Sci. Adv.* 3, e1602244.
- Bonan, G.B., 2008. Forests and climate change: forcings, feedbacks, and the climate benefits of forests. *Science* 320, 1444–1449.
- Bonan, G.B., et al., 1992. Effects of boreal forest vegetation on global climate. *Nature* 359, 716–718.
- Chen, C., et al., 2019. China and India lead in greening of the world through land-use management. *Nat. Sustain.* 2, 122–129.
- Cho, M.A., et al., 2017. Response of land surface phenology to variation in tree cover during green-up and senescence periods in the Semi-Arid Savanna of Southern Africa. *Remote Sens.* 9, 689.
- Cierner, C., et al., 2019. Higher resilience to climatic disturbances in tropical vegetation exposed to more variable rainfall. *Nat. Geosci.* 12, 174–179.
- Corlett, R.T., 2011. Impacts of warming on tropical lowland rainforests. *Trends Ecol. Evol.* 26, 606–613.
- Costanza, R., et al., 1997. The value of the world's ecosystem services and natural capital. *Nature* 387, 253–260.
- Cramer, W., et al., 2001. Global response of terrestrial ecosystem structure and function to CO₂ and climate change: results from six dynamic global vegetation models. *Glob. Change Biol.* 7, 357–373.
- Curtis, P.G., et al., 2018. Classifying drivers of global forest loss. *Science* 361, 1108–1111.
- de Jong, R., et al., 2011. Analysis of monotonic greening and browning trends from global NDVI time-series. *Remote Sens. Environ.* 115, 692–702.
- De Keersmaecker, W., et al., 2015. A model quantifying global vegetation resistance and resilience to short-term climate anomalies and their relationship with vegetation cover. *Glob. Ecol. Biogeogr.* 24, 539–548.
- Dubey, S., et al., 2015. Effect of elevated CO₂ on wheat crop: mechanism and impact. *Crit. Rev. Environ. Sci. Technol.* 45, 2283–2304.
- Fensholt, R., et al., 2012. Greenness in semi-arid areas across the globe 1981–2007 — an Earth Observing Satellite based analysis of trends and drivers. *Remote Sens. Environ.* 121, 144–158.
- Fensholt, R., et al., 2009. Evaluation of earth observation based long term vegetation trends — intercomparing NDVI time series trend analysis consistency of Sahel from AVHRR GIMMS, Terra MODIS and SPOT VGT data. *Remote Sens. Environ.* 113, 1886–1898.
- Friedl, M.A., et al., 2002. Global land cover mapping from MODIS: algorithms and early results. *Remote Sens. Environ.* 83, 287–302.
- Gao, X., et al., 2021. Vegetation responses to climate change in the Qilian Mountain Nature Reserve, Northwest China. *Glob. Ecol. Conserv.* 28, e01698.
- Gocic, M., Trajkovic, S., 2013. Analysis of changes in meteorological variables using Mann-Kendall and Sen's slope estimator statistical tests in Serbia. *Glob. Planet. Change* 100, 172–182.
- Greaver, T.L., et al., 2016. Key ecological responses to nitrogen are altered by climate change. *Nat. Clim. Change* 6, 836–843.
- Harris, I., et al., 2014. Updated high-resolution grids of monthly climatic observations – the CRU TS3.10 Dataset. *IJCli* 34 (623–642).
- Hickler, T., et al., 2008. CO₂ fertilization in temperate FACE experiments not representative of boreal and tropical forests. *Glob. Change Biol.* 14, 1531–1542.
- Holben, B.N., 1986. Characteristics of maximum-value composite images from temporal AVHRR data. *Int. J. Remote Sens.* 7, 1417–1434.
- Huete, A., et al., 2002. Overview of the radiometric and biophysical performance of the MODIS vegetation indices. *Remote Sens. Environ.* 83, 195–213.
- Jain, S., et al., 2017. Assessment of carbon neutrality and sustainability in educational campuses (CaSEC): a general framework. *Ecol. Indic.* 76, 131–143.
- Jiang, C., et al., 2017. Inconsistencies of interannual variability and trends in long-term satellite leaf area index products. *Glob. Change Biol.* 23, 4133–4146.
- Jong, R.D., et al., 2012. Trend changes in global greening and browning: contribution of short-term trends to longer-term change. *Glob. Change Biol.* 18, 642–655.
- Jong, R.D., et al., 2013. Shifts in global vegetation activity trends. *Remote Sens.* 5, 1117–1133.
- Kadiyala, K.R., 1968. A transformation used to circumvent the problem of autocorrelation. *Econometrica* 36, 93–96.
- Keenan, T.F., Riley, W.J., 2018. Greening of the land surface in the world's cold regions consistent with recent warming. *Nat. Clim. Change* 8, 825–828.
- Kendall, M.G., 1938. A new measure of rank correlation. *Biometrika* 30, 81–93.
- Lamchin, M., et al., 2020. Understanding global spatio-temporal trends and the relationship between vegetation greenness and climate factors by land cover during 1982–2014. *Glob. Ecol. Conserv.* 24, e01299.
- Liu, J., et al., 2017. Contrasting carbon cycle responses of the tropical continents to the 2015–2016 El Niño. *Science* 358, eaam5690.
- Liu, Y., et al., 2015. Spatial and temporal patterns of global NDVI trends: correlations with climate and human factors. *Remote Sens.* 7, 13233.
- Liu, Y., et al., 2012. Retrospective retrieval of long-term consistent global leaf area index (1981–2011) from combined AVHRR and MODIS data. *J. Geophys. Res. Biogeosci.* 117, G04003.
- Liu, Z., et al., 2016. Vegetation dynamics in the upper Guinean Forest region of West Africa from 2001 to 2015. *Remote Sens.* 9, 5.
- Los, S.O., 2013. Analysis of trends in fused AVHRR and MODIS NDVI data for 1982–2006: indication for a CO₂ fertilization effect in global vegetation. *Glob. Biogeochem. Cycles* 27, 318–330.
- Lucht, W., et al., 2002. Climatic control of the high-latitude vegetation greening trend and Pinatubo effect. *Science* 296, 1687–1689.
- Luo, X., et al., 2018. The impact of the 2015/2016 El Niño on global photosynthesis using satellite remote sensing. *Philos. Trans. R. Soc. B Biol. Sci.* 373.
- Mao, J., et al., 2012. Causes of spring vegetation growth trends in the northern mid-high latitudes from 1982 to 2004. *Environ. Res. Lett.* 7, 014010.
- Mashapa, C., et al., 2021. The importance of buffer zones in woody vegetation conservation in areas that combine mega-fauna and anthropogenic disturbance: the case of Save Valley landscape, south-eastern Zimbabwe. *Glob. Ecol. Conserv.* 26, e01503.
- Myinen, R.B., et al., 1997. Increased plant growth in the northern high latitudes from 1981 to 1991. *Nature* 386, 698–702.
- Pan, N., et al., 2018. Increasing global vegetation browning hidden in overall vegetation greening: insights from time-varying trends. *Remote Sens. Environ.* 214, 59–72.
- Pettorelli, N., et al., 2005. Using the satellite-derived NDVI to assess ecological responses to environmental change. *Trends Ecol. Evol.* 20, 503–510.
- Piao, S., et al., 2011. Changes in satellite-derived vegetation growth trend in temperate and boreal Eurasia from 1982 to 2006. *Glob. Change Biol.* 17, 3228–3239.
- Piao, S., et al., 2020. Characteristics, drivers and feedbacks of global greening. *Nat. Rev. Earth Environ.* 1, 14–27.
- Piao, S., et al., 2015. Detection and attribution of vegetation greening trend in China over the last 30 years. *Glob. Change Biol.* 21, 1601–1609.
- Pinzon, J., Tucker, C., 2014. A non-stationary 1981–2012 AVHRR NDVI₃ time series. *Remote Sens.* 6, 6929.

- Potter, C., et al., 1993. Terrestrial ecosystem production - a process model-based on global satellite and surface data. *Glob. Biogeochem. Cycles* 7, 811–841.
- Richards, D.R., Belcher, R.N., 2020. Global changes in urban vegetation cover. *Remote Sens.* 12.
- Samanta, A., et al., 2010. Amazon forests did not green-up during the 2005 drought. *Geophys. Res. Lett.* 37.
- Sellers, P.J., 1992. Canopy reflectance, photosynthesis, and transpiration, II. The role of biophysics in the linearity of their interdependence. *Int. J. Remote Sens.* 6, 1335–1372.
- Sitch, S., et al., 2015. Recent trends and drivers of regional sources and sinks of carbon dioxide. *Biogeosciences* 12, 653–679.
- Smith, A.M.S., et al., 2014. Remote sensing the vulnerability of vegetation in natural terrestrial ecosystems. *Remote Sens. Environ.* 154, 322–337.
- Song, X.-P., et al., 2018. Global land change from 1982 to 2016. *Nature* 560, 639–643.
- Teng, Y., et al., 2020. The effects of degradation on alpine grassland resilience: a study based on meta-analysis data. *Glob. Ecol. Conserv.* 24, e01336.
- Tucker, C.J., 1979. Red and photographic infrared linear combinations for monitoring vegetation. *Remote Sens. Environ.* 8, 127–150.
- van Schaik, E., et al., 2018. Changes in surface hydrology, soil moisture and gross primary production in the Amazon during the 2015/2016 El Niño. *Philos. Trans. R. Soc. B Biol. Sci.* 373.
- Wang, Z., et al., 2019. Changes in productivity and carbon storage of grasslands in China under future global warming scenarios of 1.5°C and 2°C. *J. Plant Ecol.* 12, 804–814.
- Wang, Z., et al., 2021. Monitoring vegetation greenness in response to climate variation along the elevation gradient in the three-river source region of China. *ISPRS Int. J. Geo-Inf.* 10, 193.
- Wang, Z., et al., 2017. Simulation of terrestrial carbon equilibrium state by using a detachable carbon cycle scheme. *Ecol. Indic.* 75, 82–94.
- Wang, Z., et al., 2016. Quantitative assess the driving forces on the grassland degradation in the Qinghai-Tibet Plateau, in China. *Ecol. Inf.* 33, 32–44.
- Wigneron, J.-P., et al., 2020. Tropical forests did not recover from the strong 2015–2016 El Niño event. *Sci. Adv.* 6, eaay4603.
- Wu, D., et al., 2014. Evaluation of spatiotemporal variations of global fractional vegetation cover based on GIMMS NDVI data from 1982 to 2011. *Remote Sens.* 6, 4217.
- Yan, T., et al., 2020. Spring phenophases of larch are more sensitive to spring warming than to year-round warming: results of a seasonally asymmetric warming experiment. *For. Ecol. Manag.* 474, 118368.
- Yuan, W., et al., 2019. Increased atmospheric vapor pressure deficit reduces global vegetation growth. *Sci. Adv.* 5.
- Zhang, Y., et al., 2017. Reanalysis of global terrestrial vegetation trends from MODIS products: browning or greening? *Remote Sens. Environ.* 191, 145–155.
- Zhu, Z., et al., 2013. Global data sets of vegetation leaf area index (LAI) 3g and Fraction of Photosynthetically Active Radiation (FPAR) 3g derived from Global Inventory Modeling and Mapping Studies (GIMMS) Normalized Difference Vegetation Index (NDVI3g) for the period 1981 to 2011. *Remote Sens.* 5, 927–948.
- Zhu, Z., et al., 2016. Greening of the earth and its drivers. *Nat. Clim. Change* 6, 791–795.
- Zhu, Z., et al., 2018. The accelerating land carbon sink of the 2000s may not be driven predominantly by the warming hiatus. *Geophys. Res. Lett.* 45, 1402–1409.